Fast Spectral-Domain Computation of Radiation Integrals Over Tilted Planes Using Unequally-Spaced Fast Laplace Transforms

Quentin Gueuning, Christophe Craeye, *Senior Member, IEEE*, and Claude Oestges, *Fellow, IEEE*

***Abstract*— A plane-wave spectrum method is presented for the fast computation of radiation integrals for source and observation plates, which can be arbitrarily tilted and separated by an intermediate-to-far-field distance. The method expedites the direct and inverse transforms between spatial and spectral domains using unequally spaced fast Laplace transforms. These fast algorithms allow one to combine fast Fourier transforms (FFTs) and contour deformation in the complex plane with controllable accuracy and computation times close to that of a single 2-D FFT. Hence, scattering interactions between plates of sizes up to thousands of wavelengths can now be computed within seconds using current desktop computers. The fast method is validated here for the case of radio propagation in a canyon street modeled with electrically large facets using the physical optics approximation.**

***Index Terms*— Contour deformation, fast Fourier transform (FFT), Green's function, nonequispaced fast Fourier transform, spectral-domain method, unequally spaced fast Laplace transforms (USFLTs).**

I. Introduction

THE fast Fourier transform (FFT) has been in use for several decades for the efficient calculation of fields radiated by complex sources. This is for instance the case for radiation from large flat apertures or for near-field to near-field or near-field to far-field transforms [1], [2]. The FFT is also often used to speed-up matrix–vector products in iterative solutions to method-of-moment (MoM) problems [3], [5]; the final goal is to compute current distributions induced in large finite antenna arrays [6] or in large printed radio frequency circuits [7]. The FFT also enables to efficiently compute array factors, either for regular or irregular arrays. In the latter case, the nonequispaced FFT (NFFT [8]) is used [9]. In a nutshell, the NFFT redistributes the irregular samples on a regular grid through a convolution. The data on the regular grid allow then the use of a standard FFT to compute the array factor, provided that deconvolution is carried out at the end, through division in the spectral domain.

As mentioned above, among the applications of the FFT in high-frequency electromagnetics, one finds near-field to near-field transforms [10], i.e., the calculation of fields in a given plane, based on the knowledge of fields in another, parallel, plane [11]. In this process, the Fourier transform of fields may be viewed as providing the coefficients of a number of plane waves composing the fields. Those plane waves are, in general, regularly sampled in the wavenumber domain. Each of them is then simply propagated up to the other plane and recomposed into fields in that new domain through an inverse Fourier transform. In passing, depending on the sign used in the complex-exponential kernel, one may swap the definitions of Fourier and inverse Fourier transforms. Henceforth, the forward transformation from the space domain to the wavenumber domain will be identified as a Fourier transform, with a positive sign in the exponential, and the backward transformation from the wavenumber domain to the space domain will be performed via an inverse Fourier transform. As explained in [23] and [24], the waves considered in this transformation are not necessarily purely propagating or purely evanescent. In general, the waves can carry both properties, as soon as a contour deformation is used in the complex wavenumber plane to carry out the Fourier transform. Such deformation is not easily made compatible with the use of the FFT algorithm. This is, for instance, the motivation for the contour-FFT (C-FFT) [12] and chirp Z transform (CZT) [13]. These techniques have been applied to layered media problems [7], [12], [14], [15].

Several applications require the knowledge of fields in observation planes that are not parallel to the source planes. For instance, this is the case for the simulation of radio channels inside and outside a built environment modeled with large planar facets [16], [17] or of the transmittance between two aperture antennas [18]. This problem has also drawn attention in optics to simulate the diffraction from the apertures composing modern laser systems [19]–[21] and in signal processing to generate holograms for 3-D television [22]. With this configuration, the exploitation of the Fourier transform appears less straightforward. Indeed, as will be detailed in Section II, the propagation of plane waves may be described in a Cartesian system of coordinates in which one axis is parallel to the straight line that joins the center of the source domain to the center of the observation domain. However, in that case, the spectral samples (i.e., in the wavenumber domain) are no

Manuscript received 23 August 2021; revised 26 February 2022; accepted 3 April 2022. Date of publication 25 April 2022; date of current version 6 October 2022. This work was supported in part by the WB-Health Program of the Walloon Region, in part by the BElgian network on STochastic modelling, analysis, design and optimization of COMmunication systems (BESTCOM), and in part by the Fonds de la Recherche Scientifique (F.R.S.-FNRS). *(Corresponding author: Quentin Gueuning.)*

Quentin Gueuning is with the Cavendish Laboratory, Astrophysics Group, University of Cambridge, Cambridge CB3 0HE, U.K. (e-mail: qdg20@cam.ac.uk).

Christophe Craeye and Claude Oestges are with the Institute of Information and Communication Technologies, Electronics and Applied Mathematics (ICTEAM), Université Catholique de Louvain, 1348 Ottignies-Louvain-la-Neuve, Belgium.

Digital Object Identifier 10.1109/TAP.2022.3168705

0018-926X © 2022 IEEE. Personal use is permitted, but republication/redistribution requires IEEE permission.
See https://www.ieee.org/publications/rights/index.html for more information.

Authorized licensed use limited to: Univ Catholique de Louvain/UCL. Downloaded on September 22,2023 at 00:11:30 UTC from IEEE Xplore. Restrictions apply.

longer regularly spaced when viewed in systems of coordinates associated with the source and observation planes. We will, hence, make use of the NFFT. More precisely, two types of NFFTs will be exploited: one that enables the fast estimation of the Fourier transform on nonregular samples and another one that enables the fast estimation of fields on a regular grid from nonregularly distributed samples in the spectral domain. More importantly, the extension of the spectral samples to the complex domain will be essential to an efficient implementation; to this end, the complex-plane extension described in [29] will be exploited. As opposed to existing formulations [19], [20] based on a purely propagating plane-wave spectrum (PWS), which exhibits numerical issues for certain rotation angles [21], the method presented here remains accurate for any configuration as long as the observation plate stands at an intermediate-to-far-field distance. As shown later, the computation times of the proposed approach are close to that of a single 2-D FFT per transformation and vectorial component. Hence, it is expected to be more efficient than methods based on the adaptive integral method [3] that uses 3-D FFTs but also than multipole approaches [4], which are more complex, as they include the calculation of translation functions, the creation of hierarchical subdomains, and interpolation and "anterpolation" steps requiring careful parametrization.

The remainder of this article first comprises a tutorial part and then applies the different reviewed techniques to the problem described above. The explanations are organized as follows. Section II provides plane-wave descriptions of radiated or scattered fields based on the convolution theorem and an extension of spectral integration to the complex plane. Section III then tackles the problem of nonparallel source and observation planes, evidencing the need for nonregularly distributed wavenumbers in the complex plane. Through the use of the vector potential, the problem will be made momentarily scalar, which simplifies both the explanations and the implementation. In the same section, both types of NFFTs are also reviewed, as well as their complex-plane extension. The developed mathematical tools are then applied to the problem at hand. Section IV shows implementation examples. Finally, the conclusions are drawn in Section V.

II. Plane-Wave Spectrum Representation of Scattered Fields

Let us consider a source plate S, an observation plate O, which is, for now, parallel to S, and a reference system of Cartesian coordinates $(\hat{\mathbf{x}}, \hat{\mathbf{y}}, \hat{\mathbf{z}})$ with the z-axis perpendicular to both plates, as shown in Fig. 1. The word "plate" is used to designate a planar domain of finite extent rather than a physical structure. The source points $\mathbf{r}_s = x_s\hat{\mathbf{x}} + y_s\hat{\mathbf{y}}$ and the observation points $\mathbf{r}_o = x_o\hat{\mathbf{x}} + y_o\hat{\mathbf{y}} + z_o\hat{\mathbf{z}}$ are, thus, lying in the planes $z = 0$ and $z = z_o$, respectively. Given electric currents $\mathbf{J}(x_s, y_s) = J_x(x_s, y_s)\hat{\mathbf{x}} + J_y(x_s, y_s)\hat{\mathbf{y}}$ on plate S, the vector field $\mathbf{A}(\mathbf{r}_o)$ is obtained from a 2-D convolution integral of $\mathbf{J}$ with the free-space scalar Green's function G

$$\mathbf{A}(\mathbf{r}_o) = \iint_S \mathbf{J}(x_s, y_s)\ G(k, R)\ \mathrm{d}x_s\mathrm{d}y_s \tag{1}$$

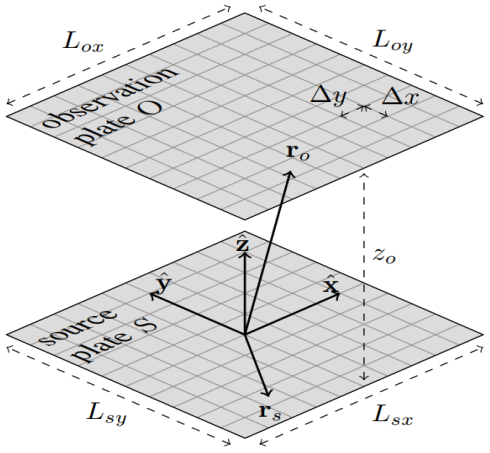


Fig. 1. Illustration of geometrical quantities for the case of an observation plate parallel to a source plate.

where $R = ((x_s - x_o)^2 + (y_s - y_o)^2 + z_o^2)^{1/2}$ is the distance between a source point and an observation point, and the free-space Green's function is defined by $G(k, R) = e^{-jkR}/(4\pi R)$ with the imaginary unit j and the wavenumber k. A harmonic time dependence $e^{j\omega t}$ is assumed and suppressed. In this article, the current distribution $\mathbf{J}$ is given on a uniform grid of side lengths L_{sx} and L_{sy} and step sizes Δx and Δy containing $N_s = N_{sx}N_{sy}$ spatial samples, and the scattered fields need to be computed at $N_o = N_{ox}N_{oy}$ observation points lying on a grid of lengths L_{ox}, L_{oy}. The electric and magnetic fields scattered away from the sources can then be expressed in terms of a magnetic vector potential $\mathbf{A}$ [25]. Their brute-force evaluation using (1) requires $O(N_oN_s)$ operations and becomes time-consuming for large electrical dimensions.

A. Spectral-Domain Formulation

In this article, we swap the convention for Fourier transforms and call (direct) Fourier transform the transformation, with a positive sign in the complex-exponential kernel, used to pass from spatial (x, y) to spectral (k_x, k_y) coordinates. Reciprocally, the backward transformation from the wavenumber domain to the space domain is identified as an inverse Fourier transform.

Since the integral (1) corresponds to a 2-D convolution, we can use the convolution theorem [26], which allows writing

$$\tilde{\mathbf{A}}(k_x, k_y, z_o) = \tilde{\mathbf{J}}(k_x, k_y)\ \tilde{G}(k_z, z_o) \tag{2}$$

where the superscript $\tilde{}$ identifies Fourier-transformed quantities, and $\mathbf{k} = k_x\hat{\mathbf{x}} + k_y\hat{\mathbf{y}} + k_z\hat{\mathbf{z}}$ is the wavevector with the z-component $k_z = (k^2 - k_x^2 - k_y^2)^{1/2}$. The Fourier transform of the current distribution $\tilde{\mathbf{J}}(k_x, k_y) = \tilde{J}_x(k_x, k_y)\hat{\mathbf{x}} + \tilde{J}_y(k_x, k_y)\hat{\mathbf{y}}$ is expressed as

$$\tilde{\mathbf{J}}(k_x, k_y) = \iint_S \mathbf{J}(x_s, y_s)\ e^{j\mathbf{k}\cdot\mathbf{r}_s}\ \mathrm{d}x_s\mathrm{d}y_s \tag{3}$$

where we have substituted the complex exponentials with $e^{j\mathbf{k}\cdot\mathbf{r}_s} = e^{jk_xx_s + jk_yy_s}$. The 2-D inverse Fourier transform $\tilde{G}$ of the free-space Green's function G has the following analytical

Authorized licensed use limited to: Univ Catholique de Louvain/UCL. Downloaded on September 22,2023 at 00:11:30 UTC from IEEE Xplore. Restrictions apply.

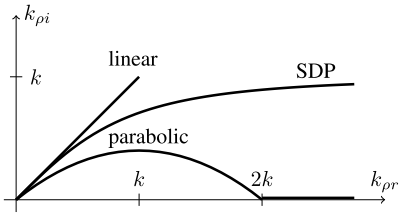


Fig. 2. Illustration of the steepest descent path (SDP), linear, and parabolic contours.

expression $\tilde{G}(k_z, z_o) = e^{-jk_z z_o}/(2jk_z)$ [11]. Knowing (2) and factorizing $e^{-jk_z z_o}$ out of $\tilde{\mathbf{A}}$ lead to the PWS representation of the magnetic vector potential $\mathbf{A}$

$$\mathbf{A}(\mathbf{r}_o) = \frac{1}{4\pi^2}\iint_{-\infty}^{+\infty} \tilde{\mathbf{A}}_0\big(k_x, k_y\big)\; e^{-j\mathbf{k}\cdot\mathbf{r}_o}\; \mathrm{d}k_x \mathrm{d}k_y \qquad (4)$$

where $\tilde{\mathbf{A}}_0(k_x, k_y) = \tilde{\mathbf{A}}(k_x, k_y, 0)$ is called the field PWS. From there, the PWSs of the magnetic and electric fields are given by [11] $\tilde{\mathbf{H}}_0(k_x, k_y) = -j\mathbf{k} \times \tilde{\mathbf{A}}_0(k_x, k_y)$ and $\tilde{\mathbf{E}}_0(k_x, k_y) = (\eta/k)\mathbf{k} \times \tilde{\mathbf{H}}_0(k_x, k_y)$, where η is the free-space impedance. It is important to note that the components $\tilde{H}_{0z}$, $\tilde{E}_{0x}$, and $\tilde{E}_{0y}$ are singular at $k_\rho = k$ via the spectral Green's function $\tilde{G}$. Hence, for these components, a numerical integration along the real coordinates (k_x, k_y) is inconvenient when the spectral samples get too close to $k_{\rho r} = (k_{xr}^2 + k_{yr}^2)^{1/2} = k$.

B. Contour Deformation Technique

To overcome numerical issues associated with the singularity of $\tilde{G}$ at $k_{\rho r} = k$, the backward transformation, from the spectral domain to the spatial domain, is usually performed using a contour deformation along $k_\rho = k_{\rho r} + jk_{\rho i} = k_{\rho r} + jf(k_{\rho r})$ [23], where the function $f(k_{\rho r})$ defines a path in the complex plane. This contour integral can be viewed as an inverse Laplace transform and reads as

$$\mathbf{A}(\mathbf{r}_o) = \frac{1}{4\pi^2}\iint_{-\infty}^{+\infty} \tilde{\mathbf{A}}_0\big(k_x, k_y\big)\; e^{-j\mathbf{k}\cdot\mathbf{r}_o}\; w\big(k_\rho\big)\; \mathrm{d}k_{xr}\mathrm{d}k_{yr} \qquad (5)$$

where the function $w(k_\rho) = k_\rho/k_{\rho r}(1 + j\mathrm{d}f/\mathrm{d}k_{\rho r})$ accounts for the contour deformation and for a polar-to-Cartesian change of variables [12]. Some well-known paths are illustrated in Fig. 2. In (5), Green's function is decomposed into inhomogeneous plane waves (IPWs), which are both propagative and evanescent [23]. Assuming a discretization of the spectral integral (9) with P plane waves, a direct computation costs PN_o operations and becomes expensive when the plates are electrically large and/or in the near-field of each other, i.e., when P is large. Hence, methods such as the C-FFT [7], [12] or the CZT [14], [15] have been proposed to speed up the computations by reformulating the integral (5) s.t. the FFT can be used again.

III. Fast Method for Tilted Plates

A fast PWS-based method needs to accelerate both the computation of the spectrum $\tilde{\mathbf{A}}_0$ from the known source current $\mathbf{J}$ with the spatial integral (3) and the scattered magnetic potential $\mathbf{A}$ from its known spectrum $\tilde{\mathbf{A}}_0$ with the spectral integral (5). The distinction between the spatial-to-spectral and spectral-to-spatial transformations is emphasized early here since, in the following, they will be evaluated using two complementary but different algorithms.

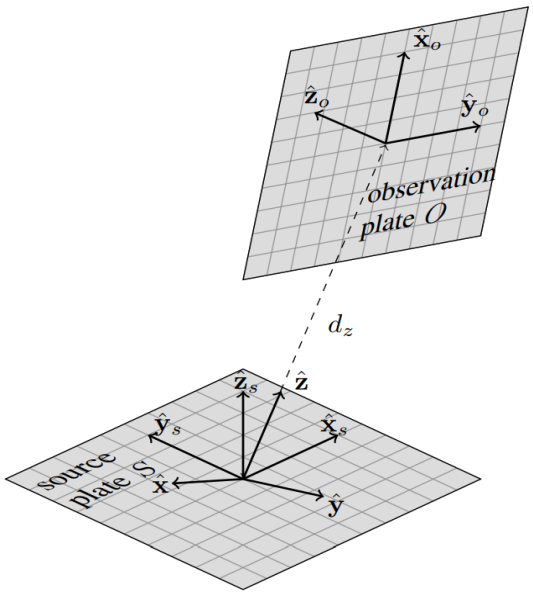


Fig. 3. Illustration of geometrical quantities for the case of tilted plates.

A. Problem Statement

Let us assume that the current distribution $\mathbf{J}$ is known on a first grid of step sizes Δx and Δy, and the vector potential $\mathbf{A}$ must be computed on a second grid with same step sizes but tilted and separated from the first grid. Defining a local system of coordinates (CS) $(\hat{\mathbf{x}}_s, \hat{\mathbf{y}}_s, \hat{\mathbf{z}}_s)$ attached to the source plane and another CS $(\hat{\mathbf{x}}_o, \hat{\mathbf{y}}_o, \hat{\mathbf{z}}_o)$ attached to the observation plane, we can express the position of the nth source point and the nth observation point, respectively, as

$$\begin{aligned} \mathbf{r}_{s,n} &= n_x \Delta x\; \hat{\mathbf{x}}_s + n_y \Delta y\; \hat{\mathbf{y}}_s \\ \mathbf{r}_{o,n} &= n_x \Delta x\; \hat{\mathbf{x}}_o + n_y \Delta y\; \hat{\mathbf{y}}_o + d_z\; \hat{\mathbf{z}} \end{aligned} \qquad (6)$$

where the double indices (n_x, n_y) are centered and have been replaced by a single index $n = N_x(n_y - 1) + n_x$ with $N_x \in \{N_{xo}, N_{xs}\}$ for compactness, $\hat{\mathbf{z}}$ is a unit vector pointing from the center of the first grid toward the center of the other grid, and d_z is the distance between those centers, as sketched in Fig. 3. The discretization of spectral integral (5) along k_x and k_y is performed using a third CS $(\hat{\mathbf{x}}, \hat{\mathbf{y}}, \hat{\mathbf{z}})$. This choice allows the use of a minimal set of IPWs [24]. Assuming a sampling with periods Δk_x, Δk_y with $P = P_x P_y$ plane waves, the complex-valued wavevector $\mathbf{k}_p$ of the pth IPW is, thus, given by

$$\mathbf{k}_p = \big(p_x \Delta k_x + jk_{xi,p}\big)\hat{\mathbf{x}} + \big(p_y \Delta k_y + jk_{yi,p}\big)\; \hat{\mathbf{y}} + k_{z,p}\hat{\mathbf{z}} \qquad (7)$$

where $p = P_x(p_y - 1) + p_x$. Generally, the CS $(\hat{\mathbf{x}}, \hat{\mathbf{y}}, \hat{\mathbf{z}})$ does neither coincide with $(\hat{\mathbf{x}}_s, \hat{\mathbf{y}}_s, \hat{\mathbf{z}}_s)$ nor $(\hat{\mathbf{x}}_o, \hat{\mathbf{y}}_o, \hat{\mathbf{z}}_o)$. Hence, the dot product $\mathbf{k} \cdot \mathbf{r}$ in (3) and (4) must be computed by reexpressing the wavevector $\mathbf{k}$ and the position $\mathbf{r}$ into

Authorized licensed use limited to: Univ Catholique de Louvain/UCL. Downloaded on September 22,2023 at 00:11:30 UTC from IEEE Xplore. Restrictions apply.

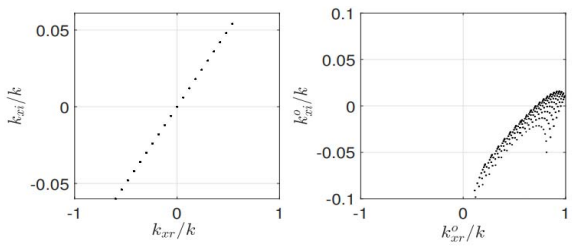


Fig. 4. Irregular distribution of the IPW samples from a change of CS $(\hat{\mathbf{x}}, \hat{\mathbf{y}}, \hat{\mathbf{z}})$ to $(\hat{\mathbf{x}}_o, \hat{\mathbf{y}}_o, \hat{\mathbf{z}}_o)$ resulting from a rotation in the xz plane by $\pi/4$.

a common CS. For instance, the exponential factor in (4) evaluated at $\mathbf{r}_{o,n}$ becomes

$$e^{-j\mathbf{k}_p\cdot\mathbf{r}_{o,n}} = e^{-jk_z d_z}\ e^{-jk_{ox,p}n_x\Delta x}\ e^{-jk_{oy,p}n_y\Delta y} \tag{8}$$

where the xy coordinates of $\mathbf{k}_p$ in the CS $(\hat{\mathbf{x}}_o, \hat{\mathbf{y}}_o, \hat{\mathbf{z}}_o)$ are given by

$$\begin{bmatrix} k_{ox,p} \\ k_{oy,p} \end{bmatrix} = \begin{bmatrix} \hat{\mathbf{x}}_o\cdot\hat{\mathbf{x}} & \hat{\mathbf{x}}_o\cdot\hat{\mathbf{y}} & \hat{\mathbf{x}}_o\cdot\hat{\mathbf{z}} \\ \hat{\mathbf{y}}_o\cdot\hat{\mathbf{x}} & \hat{\mathbf{y}}_o\cdot\hat{\mathbf{y}} & \hat{\mathbf{y}}_o\cdot\hat{\mathbf{z}} \end{bmatrix} \begin{bmatrix} p_y\Delta k_y + jk_{yi,p} \\ p_x\Delta k_x + jk_{xi,p} \\ k_{z,p} \end{bmatrix}. \tag{9}$$

Similar relations are obtained for the plane-wave exponential in (3). Note that, although the spectral integral (5) is discretized s.t. the IPWs have real variables k_{xr}, k_{yr} distributed over regular grids, the rotated spectral coordinates k_{sx}, k_{sy}, k_{ox}, and k_{oy} have both real and imaginary parts nonuniformly spaced over the complex plane. This effect is illustrated in Fig. 4 considering a linear contour of slope 0.1 for which we have $k_{xi} = 0.1k_{xr}$ and a rotation by $\pi/4$ in the xz plane. As expected, one can see that the rotated samples $k_{ox,p}$ are nonregularly spread over the complex plane. The CFFT and the CZT do not inherently deal with irregularly spaced complex-valued samples. Hence, they cannot be applied here. Instead, we first exploit a complex-plane extension of a family of methods specifically invented to accelerate Fourier transforms with nonregular sampling, namely, the NFFT [8]. Then, we introduce a complex-plane extension of these methods, inspired from [29].

In order to alleviate the explanations, the fast algorithm is presented first in the scalar case using an arbitrary function $g(x, y)$ and its spectrum $\tilde{g}(k_x, k_y)$. Indeed, one can infer that the backward transform (4), expressing the scattered field from its IPW spectrum, corresponds for each tangential component to the computation of g from its spectrum $\tilde{g}$ using

$$g(x,y) = \frac{1}{4\pi^2}\iint_{-\infty}^{+\infty} \tilde{g}\big(k_x,k_y\big) \times e^{-jk_x x - jk_y y}\ w\big(k_\rho\big)\ \mathrm{d}k_{xr}\mathrm{d}k_{yr}. \tag{10}$$

Reciprocally, the transform (3), used to derive the IPW spectrum from the current, involves two times the computation of the spectrum of g from its analytical expression

$$\tilde{g}\big(k_x,k_y\big) = \iint_S g(x,y)\ e^{jk_x x + jk_y y}\ \mathrm{d}x\mathrm{d}y. \tag{11}$$

The complete vectorial transformation using the vector fields $\mathbf{A}$ and $\mathbf{J}$ is presented later in Section III-D.

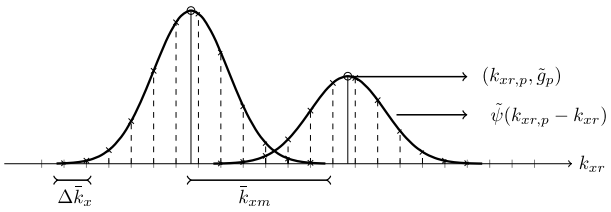


Fig. 5. Unidimensional redistribution of an irregular sample $\tilde{g}_p$ located at $k_{xr,p}$ on a regular grid of step size $\Delta\bar{k}_x$ using a Gaussian window function $\tilde{\psi}$ truncated at k_{xm}.

B. Reminder on the Nonequispaced Fast Fourier Transform

Dutt and Rockhlin [8] derived three types of NFFT algorithms depending on whether samples are nonuniformly spaced only in the domain of destination (type 1), the domain of departure (type 2), or both domains (type 3). At this point, the coordinates are real numbers, and the contour deformation is left aside until Section III-C. We briefly recall the first two types, which will be used later in this article.

For type 1, let us assume that the spectrum $\tilde{g}$ has been priorly sampled nonuniformly over the $k_x k_y$ domain s.t. its sampled version $\tilde{g}_s$ can be represented with a 2-D comb

$$\tilde{g}_s\big(k_{xr},k_{yr}\big) = \sum_p\ \tilde{g}_p\ \delta\big(k_{xr}-k_{xr,p}\big)\ \delta\big(k_{yr}-k_{yr,p}\big) \tag{12}$$

where $\tilde{g}_p = \tilde{g}(k_{xr,p}, k_{yr,p})$ and δ is Dirac's delta. $(k_{xr,p}, k_{yr,p})$ are nonuniformly distributed over the (so far real) (k_x, k_y) plane. The inverse Fourier transform of $\tilde{g}_s$ corresponds to a sum of complex exponentials

$$g_s(x,y) = \frac{1}{4\pi^2}\ \sum_p\ \tilde{g}_p\ e^{-jk_{xr,p}x - jk_{yr,p}y}. \tag{13}$$

The type-1 NFFT rapidly computes this type of sum on a spatial grid by first rapidly redistributing the nonuniform samples $\tilde{g}_p$ over a uniform grid $(k_{xr}, k_{yr}) = (q_x\Delta\bar{k}_x, q_y\Delta\bar{k}_y)$ with integers q_x and q_y and by then performing the inverse Fourier transform from this spectral grid to the spatial grid $(x, y) = (n_x\Delta x, n_y\Delta y)$ using the FFT. In our applications, the spatial grid will correspond to that of the observation points (see Section III-D). The gridding step is accomplished by convolving the sampled function $\tilde{g}_s$ with an arbitrary window function $\tilde{\psi}$

$$\tilde{g}_\psi\big(k_{xr},k_{yr}\big) = \sum_p\ \tilde{g}_p\ \tilde{\psi}\big(k_{xr}-k_{xr,p}, k_{yr}-k_{yr,p}\big). \tag{14}$$

Then, by virtue of the convolution theorem, the inverse Fourier transform of $\tilde{g}_\psi$ is written as

$$g_s(x,y)\ \psi(x,y) = \frac{1}{4\pi^2}\iint_{-\infty}^{+\infty} \tilde{g}_\psi\big(k_{xr},k_{yr}\big) \times e^{-jk_{xr}x - jk_{yr}y}\ \mathrm{d}k_{xr}\mathrm{d}k_{yr} \tag{15}$$

which means that g_s can be reexpressed as an inverse Fourier transform, followed by a division by ψ. The spectral integral in (15) is usually approximated with rectangles of lengths $\Delta\bar{k}_x$ and $\Delta\bar{k}_y$. The convolution (14) can be regarded as redistributing the nonuniform samples $\tilde{g}_p$ on the regular set of points $(q_x\Delta\bar{k}_x, q_y\Delta\bar{k}_y)$. The convolution product can be

Authorized licensed use limited to: Univ Catholique de Louvain/UCL. Downloaded on September 22,2023 at 00:11:30 UTC from IEEE Xplore. Restrictions apply.

computed efficiently using a rapidly decaying window function $\tilde{\psi}$, as illustrated in Fig. 5, with a Gaussian window. In this case, only a few surrounding samples p will contribute significantly to g_ψ at a given point q on the grid. The function $\tilde{\psi}$ should, however, be wide enough not to preclude the redistribution in the first place. Finally, the 2-D FFT, denoted by $FFT2$ hereafter, is applied to evaluate (15)

$$g_{s,n} \simeq \frac{1}{\bar{L}_x \bar{L}_y \psi_n} \; FFT2\{\tilde{g}_{\psi,q}\} \tag{16}$$

where $\psi_n = \psi(n_x \Delta x, n_y \Delta y)$ and $g_{s,n} = g_s(n_x \Delta x, n_y \Delta y)$. Naturally, the truncation limit and the discretization rate of the Fourier integral (15) must depend on the decay rate and the bandwidth of $\tilde{g}_\psi$.

Another type of NFFT can be used to accelerate the computations of the Fourier transform of a uniformly sampled function

$$g_s(x, y) = \sum_n \; g_n \; \delta(x - n_x \Delta x) \; \delta\big(y - n_y \Delta y\big) \tag{17}$$

at a set of irregularly spaced wavenumbers $(k_{xr,p}, k_{yr,p})$. We consider here the Fourier transform of g_s given by

$$\tilde{g}_s\big(k_{xr}, k_{yr}\big) = \sum_n \; g_n \; e^{jk_{xr} n_x \Delta x + jk_{yr} n_y \Delta y}. \tag{18}$$

The fast algorithm, qualified as type 2 in [8], is similar to a local linear interpolation, which evaluates the spectrum $\tilde{g}_s$ at any coordinates $(k_{xr,p}, k_{yr,p})$ from a small number of nearby samples taken over a grid $(q_x \Delta \bar{k}_x, q_y \Delta \bar{k}_y)$. It expresses the spectrum $\tilde{g}_s$ as a convolution between a (so far unknown) spectral function $\tilde{g}_\psi$ and a given kernel $\tilde{\psi}$

$$\tilde{g}_s\big(k_{xr,p}, k_{yr,p}\big) = \iint_{-\infty}^{+\infty} \tilde{g}_\psi\big(k_{xr}, k_{yr}\big) \times \tilde{\psi}\big(k_{xr} - k_{xr,p}, k_{yr} - k_{yr,p}\big) \; \mathrm{d}k_{xr} \mathrm{d}k_{yr}. \tag{19}$$

The function $\tilde{g}_\psi$ must now be expressed in terms of the known spatial function g_s. Again, by means of the convolution theorem, the inverse Fourier transform of this convolution product is $g_s(x, y) = \psi(x, y) \; g_\psi(x, y)$. From there, g_ψ can be isolated, and given the definition (17) of g_s as a comb function, its Fourier transform $\tilde{g}_\psi$ is expressed as

$$\tilde{g}_\psi\big(k_{xr}, k_{yr}\big) = \sum_n \; \frac{g_n}{\psi_n} \; e^{jk_{xr} n_x \Delta x + jk_{yr} n_y \Delta y}. \tag{20}$$

One must note that relations (19) and (20) are exact. However, in practice, the convolution integral must be truncated and discretized at rates $\Delta \bar{k}_x$ and $\Delta \bar{k}_y$. Defining the frame function $\tilde{\psi}_q(k_{xr}, k_{yr}) = \tilde{\psi}(k_{xr} - q_x \Delta \bar{k}_x, k_{yr} - q_y \Delta \bar{k}_y)$, we have

$$\tilde{g}_s\big(k_{xr}, k_{yr}\big) \simeq \sum_q \; \tilde{c}_q \; \tilde{\psi}_q\big(k_{xr}, k_{yr}\big) \tag{21}$$

with $\tilde{c}_q = \Delta \bar{k}_x \Delta \bar{k}_y \tilde{g}_\psi(q_x \Delta \bar{k}_x, q_y \Delta \bar{k}_y)$. This ressembles a linear decomposition of $\tilde{g}_s$ using a set of basis functions $\tilde{\psi}_q$ with expansion coefficients given by $\tilde{c}_q$. When the window function $\tilde{\psi}$ exhibits a fast decay, only a few local frames $\tilde{\psi}_q$ of indices q close to $(k_{xr,p}/\Delta \bar{k}_x, k_{yr,p}/\Delta \bar{k}_y)$ are needed to interpolate $\tilde{g}_s$ accurately. The coefficients $\tilde{c}_q$ can be rapidly computed from (20) with

$$\tilde{c}_q = \frac{4\pi^2}{\Delta x \Delta y} \; \mathrm{IFFT2}\left\{\frac{g_n}{\psi_n}\right\} \tag{22}$$

where IFFT2 stands for the inverse 2-D FFT.

C. Unequally Spaced Fast Laplace Transform

The NFFT algorithms have been extended in [29] to deal with sums (13) and (20) in which the nonuniform spectral samples $(k_{xr,p} + jk_{xi,p}, k_{yr,p} + jk_{yi,p})$ are complex numbers. In our application, given the contour deformations in the complex spectral plane (see Section II-B), such an extension with complex wavenumber is necessary. The corresponding algorithms have been renamed the unequally spaced fast Laplace transforms (USFLTs) in [29].

These algorithms are easily derived from our previous explanations. Indeed, the type 1 USFLT is derived by assuming that the spectrum $\tilde{g}_s$ in (12), to be Fourier-transformed, consists of a collection of Dirac deltas shifted at complex coordinates (k_{xp}, k_{yp})

$$\tilde{g}_s\big(k_{xr}, k_{yr}\big) = \sum_p \; \tilde{g}_p \; \delta\big(k_{xr} - k_{x,p}\big) \; \delta\big(k_{yr} - k_{y,p}\big). \tag{23}$$

Hence, its inverse Fourier transform g_s is computed by first redistributing the complex-valued nonuniform samples onto a grid on the real plane (k_{xr}, k_{yr}) using

$$\tilde{g}_\psi\big(k_{xr}, k_{yr}\big) = \sum_p \; \tilde{g}_p \; \tilde{\psi}\big(k_{xr} - k_{x,p}, k_{yr} - k_{y,p}\big) \tag{24}$$

and then by evaluating g_s using (16). The only difference between (12) and (24) is that the real coordinates $(k_{xr,p}, k_{y,rp})$ have been replaced by the complex ones $(k_{x,p}, k_{y,p})$. Similarly, the type 2 USFLT simply consists of an analytical continuation of the decomposition (21)

$$\tilde{g}_s\big(k_x, k_y\big) \simeq \sum_q \; \tilde{c}_q \; \tilde{\psi}_q\big(k_x, k_y\big) \tag{25}$$

where $\tilde{\psi}_q(k_x, k_y) = \tilde{\psi}(k_x - q_x \; \Delta \bar{k}_x, k_y - q_y \; \Delta \bar{k}_y)$ with $k_x = k_{xr} + jk_{xi}$ and $k_y = k_{yr} + jk_{yi}$ now being complex-valued. The parameterization of the USFLTs implemented with Gaussian windows is provided in the Appendix. In both types, the window functions $\tilde{\psi}$ are now evaluated at complex arguments. As shown in Appendix, this implies that wider windows must be used, as compared to a real-axis integration, which, in turn, leads to a larger number M_x of frames for a given error level ϵ. Despite this constraint, we will show in Section IV that the computational cost of the USFLT remains close to that of a single FFT when applied to the computation of scattered fields.

D. Fast Computation of Vector Fields

We now explain how these USFLT algorithms can help us to accelerate the computation of the vector potential $\mathbf{A}$ on a tilted observation plate O from known electric currents $\mathbf{J}(\mathbf{r}_s)$ on a source plate S. As mentioned in the preamble III-A, it is assumed that the current distribution consists of a collection

Authorized licensed use limited to: Univ Catholique de Louvain/UCL. Downloaded on September 22,2023 at 00:11:30 UTC from IEEE Xplore. Restrictions apply.

of point sources of complex amplitude $\mathbf{J}_n$ located on a spatial grid of step size Δx, Δy. Hence, its spectrum $\tilde{\mathbf{J}}$ is given by

$$\tilde{\mathbf{J}}(k_{sx}, k_{sy}) = \sum_n \mathbf{J}_n \; e^{jk_{sx}n_x\Delta x + jk_{sy}n_y\Delta y} \tag{26}$$

where (k_{sx}, k_{sy}) are the spectral coordinates reexpressed in the source CS $(\hat{\mathbf{x}}_s, \hat{\mathbf{y}}_s, \hat{\mathbf{z}}_s)$. Comparing (26) with (18) reveals that the type 2 USFLT can be used to compute the two tangential components of $\tilde{\mathbf{J}}$ at any of the nonregularly distributed coordinates $(k_{sx,p}, k_{sy,p})$. Furthermore, knowing that $\tilde{\mathbf{A}}_0 = \tilde{\mathbf{J}}/(2jk_z)$, one can directly decompose the PWS into a set of frame functions, as described in (21)

$$\tilde{\mathbf{A}}_0(k_{sx}, k_{sy}) \simeq \frac{1}{2jk_z} \sum_q \tilde{\mathbf{c}}_q \; \tilde{\psi}_q(k_{sx}, k_{sy}) \tag{27}$$

with the vectorial coefficients computed with $\tilde{\mathbf{c}}_q = 4\pi^2/(\Delta x \Delta y)\text{IFFT2}\{\mathbf{J}_n/\psi_n\}$. One must distinguish between the z-component of the wavevector k_z in (27), expressed in the reference CS $(\hat{\mathbf{x}}, \hat{\mathbf{y}}, \hat{\mathbf{z}})$, and the source coordinates (k_{sx}, k_{sy}), expressed in $(\hat{\mathbf{x}}_s, \hat{\mathbf{y}}_s, \hat{\mathbf{z}}_s)$. Once the coefficients $\tilde{\mathbf{c}}_q$ are rapidly computed with IFFTs, the values $\tilde{\mathbf{A}}_{0,p} = \tilde{\mathbf{A}}_0(k_{sx,p}, k_{sy,p})$ of the PWS are then evaluated with (27) at any point p using a small number of frames $\tilde{\psi}_q$.

From there, the vector potential $\mathbf{A}_n = \mathbf{A}(\mathbf{r}_{o,n})$ is computed on the regular observation grid at coordinates $\mathbf{r}_{o,n}$, as given in (6), by discretizing the spectral integral (5) with periods Δk_x and Δk_y using $P = P_x P_y$ plane waves. Using $\tilde{\mathbf{A}}_p = \tilde{\mathbf{A}}(k_{sx,p}, k_{sy,p})e^{-jk_{z,p}d_z}$, this yields

$$\mathbf{A}_n \simeq \frac{1}{4\pi^2} \sum_{p=1}^{P} w_p \; \tilde{\mathbf{A}}_p \; e^{-jk_{ox,p}n_x\Delta x - jk_{oy,p}n_y\Delta y} \tag{28}$$

where $w_p = \Delta k_x \Delta k_y w(k_{\rho,p})$ can be regarded as integration weights and the coordinates $(k_{ox,p}, k_{oy,p})$ are expressed in the CS $(\hat{\mathbf{x}}_o, \hat{\mathbf{y}}_o, \hat{\mathbf{z}}_o)$ attached to the observation plate. One can check that (28) is similar to the canonical sum (13) used to explain the type 1 USFLT. Hence, by analogy with (16), the vector potential can be rapidly computed with

$$\mathbf{A}_n \simeq \frac{1}{\bar{L}_x \bar{L}_y \psi_n} \; FFT2\{\tilde{\mathbf{A}}_{\psi,q}\}. \tag{29}$$

The set $\tilde{\mathbf{A}}_{\psi,q}$ corresponds to the redistributed samples of $\tilde{\mathbf{A}}_p$ over a regular grid $(q_x\Delta\bar{k}_x, q_y\Delta\bar{k}_y)$, which, from (24), are obtained with $\tilde{\mathbf{A}}_{\psi,q} = \sum_p w_p \tilde{\mathbf{A}}_p \tilde{\psi}_q(k_{ox,p}, k_{oy,p})$. This concludes the description of the fast algorithm used to evaluate the vector potential samples $\mathbf{A}_n$ from a set of point sources $\mathbf{J}_n$ as the computations involve only FFTs and efficient convolutions.

E. Computational Cost

The sampling steps are chosen as $\Delta\bar{k}_x = 2\pi/\bar{L}_x$ and $\Delta\bar{k}_y = 2\pi/\bar{L}_y$ with the extended lengths $\bar{L}_x = \bar{\nu}_x L_x$ and $\bar{L}_y = \bar{\nu}_y Ly$ being slightly larger than the original lengths L_x and L_y of the spatial domain of interest and with the number of points $\bar{N}_x = \bar{\nu}_x N_x$ and $\bar{N}_y = \bar{\nu}_y N_y$ being powers of 2 to satisfy the FFT requirements. The number of frames M_x and M_y, needed to evaluate the coefficients in (27) or to redistribute the PWS on a regular grid, can be made asympotically independent of the electrical size kL_x and kL_y of the plates. This means that the complexity of the convolution step can be linear w.r.t. the electrical size of the plate, i.e., $M_x M_y N_O(kL_x kL_y)$. The number of frames M_x is given by

$$M_x = \frac{2\bar{k}_{xm}}{\Delta\bar{k}_x} = \frac{2\bar{k}_{xm}L_x}{\bar{\nu}_x} \tag{30}$$

with the truncation limit $\bar{k}_{xm}$ parameterized with (35) in Appendix for the case of Gaussian windows. From (30) and (35), one can infer that M_x depends roughly on $\mu_x L_x^2$ with the variance μ_x also varying with L_x through $\mu_x \propto k_{xim}/L_x$ where k_{xim} is the maximum imaginary part among the nonuniform samples. Hence, for M_x and M_y to be asympotically independent of kL_x and kL_y, the contour deformation must be chosen s.t. k_{xim} and k_{yim} decrease with $1/L_x$ and $1/L_y$. We will show in Section IV that this condition is easily achieved, for any parallel plate configurations and for tilted plates that lie in the intermediate-to-far-field of each other, by choosing a contour height that is low enough. This does unfortunately not hold for near-field configuration since the imaginary parts of the rotated coordinates k_{oxi}, k_{oyi}, k_{sxi}, and k_{syi} do not necessarily decrease with k_{xi} and k_{yi} for plane waves with $k_{\rho,r} > k$.

IV. Numerical Results

In this section, we first characterize the computational cost of the fast method by analyzing the type 1 USFLT (see Section III-C) for the evaluation of the scalar Green's function on either a parallel or a tilted observation plate. The cost for the type 2 USFLT is similar. Then, we present two numerical examples using the physical optics (PO) approximation where the computation of the vector fields from the PO currents is accelerated using the fast method described in Section III-D. The simulations are carried out with MATLAB [34] using a PC with four cores, 16 GB RAM, and Processor Intel[1] Core[2] i5-3570 CPU @ 3.4 GHz. The gridding step is single-threaded and implemented in C, while the FFTs are multithreaded via the FFTW library [35] called by MATLAB.

A. Fast Evaluation of the Scalar Green's Function

The scalar Green's function G can be evaluated numerically on a uniform grid $(n_x\Delta x, n_y\Delta y)$ of N observation points at coordinates $\mathbf{r}_{o,n}$ using

$$G_n \simeq \frac{1}{4\pi^2} \sum_{p=1}^{P} w_p \; \tilde{G}_p \; e^{-jk_{ox,p}n_x\Delta x - jk_{oy,p}n_y\Delta y} \tag{31}$$

where $\tilde{G}_p = \tilde{G}(k_{z,p}, d_z)$ is the pth sample of the spectral Green's function and $G_n = G(k, R_n)$ with $R_n = ||\mathbf{r}_{o,n}||$ being the distance from the origin to the nth observation point. The sum (31) can be simply retrieved by replacing, in (28), the vector potential $\mathbf{A}_n$ and its spectrum $\tilde{\mathbf{A}}_p$ with G_n and $\tilde{G}_p$, respectively. The computation of (31) will be accelerated with the type 1 USFLT in two different scenarios: an in-plane near-field evaluation, as encountered in the scattering analysis

[1]Registered Trademark.
[2]Trademarked.

Authorized licensed use limited to: Univ Catholique de Louvain/UCL. Downloaded on September 22,2023 at 00:11:30 UTC from IEEE Xplore. Restrictions apply.

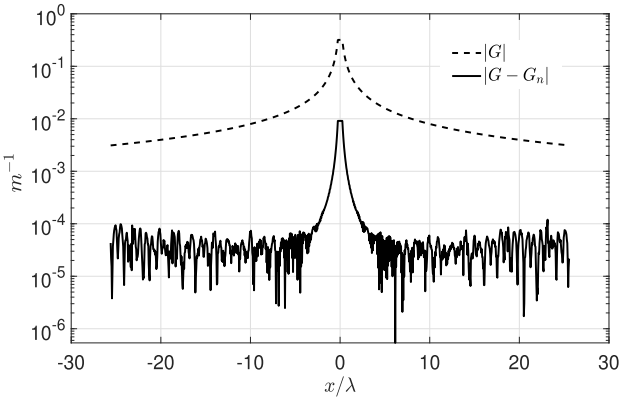


Fig. 6. In-plane evaluation of the Green's function: the amplitude $|G|$ and the absolute errors $|G - G_n|$ are shown for an observation plate of size 50λ until a distance $\rho_{\min} = \lambda/5$.

of printed circuits, and an intermediate-field evaluation on a tilted observation plate, resembling the scattering interactions between electrically large facets.

1) In-Plane Evaluation: Let us first assume an observation plate lying in the z-plane at $d_z = 0$ and with an observation CS $(\hat{\mathbf{x}}_o, \hat{\mathbf{y}}_o, \hat{\mathbf{z}}_o)$ corresponding to the reference CS $(\hat{\mathbf{x}}, \hat{\mathbf{y}}, \hat{\mathbf{z}})$. In this scenario, one seeks to reconstruct G on this observation plate up to a minimum radial distance $\rho_{\min} > 0$. When this distance $\rho_{\min}$ is small compared to the wavelength, a contour f returning to the real axis $k_{\rho r}$ is typically selected [27] along with truncation limits extending far beyond the visible spectrum to accurately reconstruct the singular behavior of G at a small distance ρ. Here, we use the parabolic path [12] depicted in Fig. 2 and parameterized with a contour height ak. The truncation limits k_{xm} and k_{ym} are selected with [32, eq. (6)]. The spatial and spectral periods are set to the Nyquist rates $\Delta x = \pi/k_{xm}$, $\Delta y = \pi/k_{ym}$, $\Delta k_x = 2\pi/L_{ox}$, and $\Delta k_y = 2\pi/L_{oy}$. Similar to Hubert *et al.* [7], we then select the minimum contour height ak leading to a targeted error level ϵ. This helps to reduce the cost of the gridding step since the number M of frames decreases with ak, as explained in Section III-E. Moreover, the redistribution of the purely real spectral samples, i.e., these with $k_{\rho,r} > 2k$ when the parabolic contour has returned on the real axis, is computed here separately using the built-in function "conv2" of MATLAB. We consider now an example with a minimum distance $\rho_{\min} = \lambda/5$ and a square plate of sizes $L_{ox} = L_{oy} = 50\lambda$. From there, the spectral periods are selected as $\Delta k_x = \Delta k_y = 0.12$. For a target error of -30 dB, i.e., $\epsilon = 0.03$, the truncation limits must be set to $k_{xm} = k_{ym} = 10k$, and thus, the spatial periods are given by $\Delta x = \Delta y = \lambda/20$. The resulting number of spatial samples is $N = 1024^2$. The contour height ak is chosen as $0.015k$. For these parameters, the required number of frames is equal to $M = 8^2$. Green's function G and the absolute error $G - G_n$ are shown in Fig. 6 for an observation path along the x-axis at $y = 0$. The peak appearing in the error at low lateral distance x results from the truncation of the spectral integral, while the constant level of the error at higher distances is caused by its discretization. One can observe that the -30 dB criterion is satisfied for every point along this observation path. The computation times of the gridding step and the FFT step are, respectively, 0.09 and 0.07 s. Hence, the gridding step takes about the same time as the FFT.

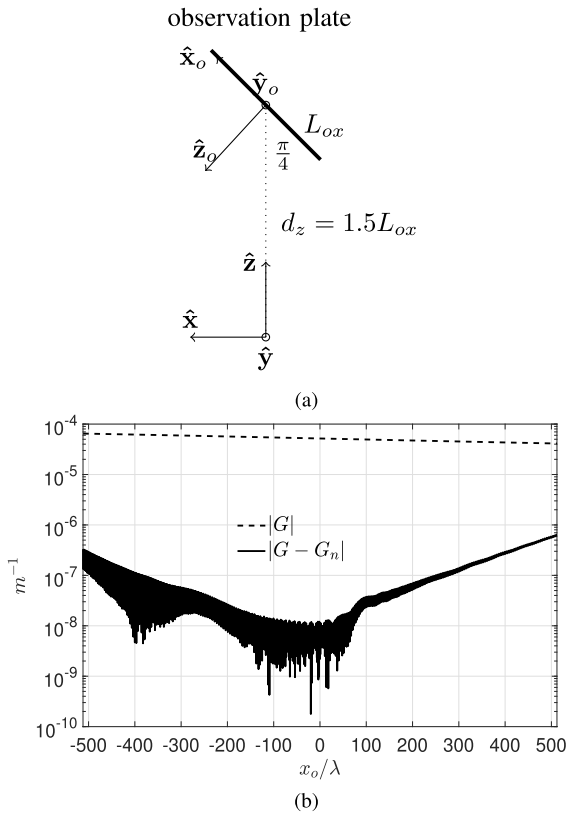


Fig. 7. Intermediate-field evaluation of Green's function on a tilted plate: the amplitude $|G|$ and the absolute error $|G - G_n|$ are shown in (b) for an observation plate of size 1024λ rotated by $\pi/4$ in the xz plane and separated by a distance $d_z = 1.5L_{xo}$ from the origin, as sketched in (a).

2) Intermediate-Field Evaluation on a Tilted Plate: We consider here the scenario shown in Fig. 7(a) in which an observation plate is rotated by $\pi/4$ in the xz plane and whose center is at a distance $d_z = 1.5\ L_{ox}$ from the origin. When the plate is electrically large, i.e., $L_{ox}, L_{oy} \gg \lambda$, this case corresponds to an intermediate-field evaluation since the distance d_z is larger than the plate dimension L_{ox} but much smaller than the far-field distance $4L_{ox}^2/\lambda$. A numerical experiment is carried out by increasing the plate size exponentially as $L_{ox} = 2^n$ with $n \in [6, 10]$. The mesh size is fixed to $\Delta x = \Delta y = \lambda/4$. For this intermediate-field case, we use here an unclosed linear contour of slope a, as shown in Fig. 2. The contour slope a is chosen to minimize the cost MP of the gridding step of the USFLT. The truncation limits k_{xm} and k_{ym} and the periods Δk_x and Δk_y are selected using the sampling rules for linear contours presented in [24], and the target accuracy is set to $\epsilon = 10^{-2}$. One can observe in Fig. 7(b) that, as expected, the reconstructed Green's function is accurate down to two digits for the largest plate of size $L_{ox} = 1024\lambda$. The maximum errors over the observation plate and the computation times of the gridding step and the FFT step of the USFLT are provided in Table I for every plate dimension. This table shows that the time spent for the gridding step is similar to that needed for the FFT. Hence, for

Authorized licensed use limited to: Univ Catholique de Louvain/UCL. Downloaded on September 22,2023 at 00:11:30 UTC from IEEE Xplore. Restrictions apply.

TABLE I

MAXIMUM RELATIVE ERROR AND COMPUTATION TIMES FOR THE GRIDDING STEP AND THE FFT STEP OF THE USFLT FOR THE SCENARIO IN FIG. 7 WITH PLATES OF INCREASING SIZE L_{ox}

L_{ox}/λ	2^6	2^7	2^8	2^9	2^{10}
$\bar{\nu}_x N_{ox}$	2^9	2^{10}	2^{11}	2^{12}	2^{13}
Rel. error max	0.01	0.02	0.03	0.02	0.02
Gridding (secs)	0.008	0.03	0.1	0.5	2.2
FFT (secs)	0.006	0.02	0.09	0.4	2

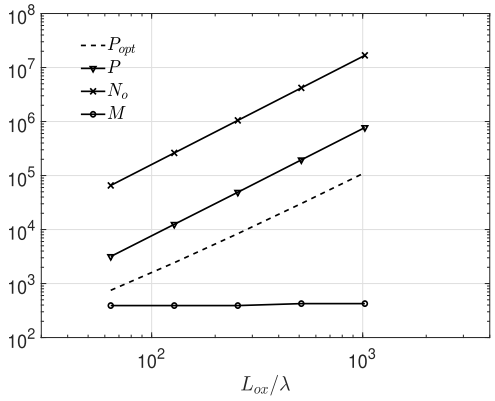


Fig. 8. Intermediate-field evaluation of Green's function on a tilted plate: comparison of the Nyquist number, the number P of plane-waves, the number N of spatial samples, and the number of grid points M when increasing the plate size L_{ox} in the sketch in Fig. 7(a).

this intermediate-field evaluation, the total time for the USFLT should be close to twice that of a classical FFT. The evolution of the number P of plane waves, the number M of frames, and the number N of spatial samples is shown in Fig. 8. From these curves, one can infer that P and N both increase quadratically with L_x, while M remains constant. As discussed earlier in Section III-E, this is achieved using a contour slope a, which is inversely proportional to L_{ox}. We must recall that the optimal contour slope selected here leads to a minimum cost MP but not to a minimum number P_{opt} of plane waves. This number P_{opt}, as derived in [24], is also plotted in Fig. 8 for comparison with P.

B. Fast Computation of the PO Radiation Integral

In this example, we assume that a point source oriented along $\hat{\mathbf{z}}$ illuminates a perfect electric conductor (PEC) plate with a magnetic field $\mathbf{H}^i(\mathbf{r})$, as sketched in Fig. 9(a). The electric surface current induced on the surface of the plate is then approximated using the PO formula $\mathbf{J}(\mathbf{r}) \simeq 2\hat{\mathbf{n}} \times \mathbf{H}^i(\mathbf{r})$. A comparison is then made between the backscattered fields computed on a perpendicular observation plate using either the fast spectral-domain method or a brute-force spatial-domain integration of the radiation integrals. The source and observation plates, both of size 20λ, are discretized using sampling steps $\Delta x = \Delta y = \lambda/4$, as typically done when computing multiple scattering PO interactions. This leads to $N = 6400$ points per plate. Again, we use here a linear contour deformation, and the target error is $\epsilon = 10^{-3}$. Fig. 9(b) shows

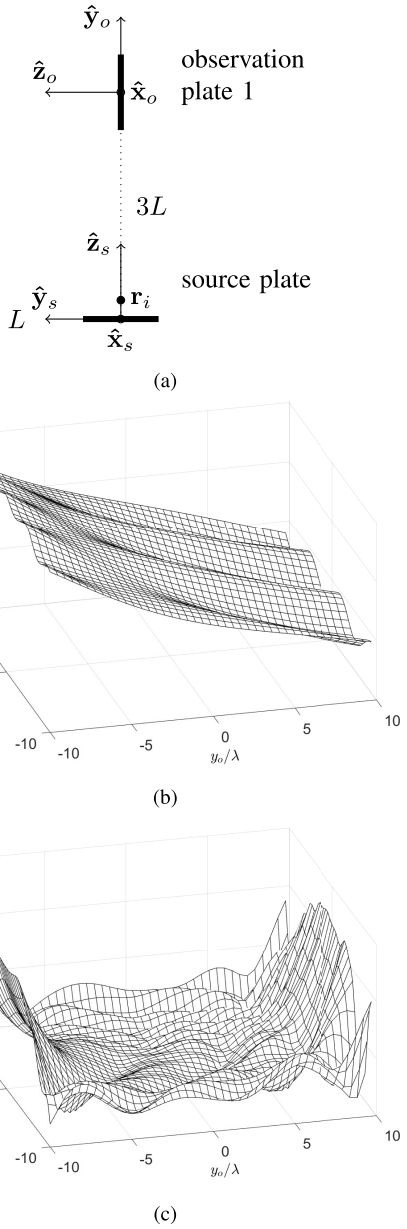


Fig. 9. Fast computation of the PO integral: (b) magnitude of the backscattered field and (c) relative error of the fast method are plotted for the scattering scenario depicted in (a).

the magnitude $||\mathbf{E}||_2$ of the backscattered electric field and the absolute error computed numerically with $||\mathbf{E}(\mathbf{r}) - \mathbf{E}^u(\mathbf{r})||_2$, where $\mathbf{E}^u$ is the field reconstructed with the fast method. As expected, one can see in Fig. 9(b) that the field evaluated with the fast method is reconstructed down to less than three digits of accuracy. The relative error is slightly higher on the edges of the observation domain. The required number P of plane waves and the number of frames M are $P = 550$ and $M = 72$, respectively. The computation times of the spatial-domain integration and the USFLT-based method are 30 and 0.2 s, respectively. Hence, the fast method provides a speed-up factor of two orders of magnitude.

C. Radio Propagation in a Canyon

The fast USFLT-based method finds typical applications for the characterization of radio channels inside a building or

Authorized licensed use limited to: Univ Catholique de Louvain/UCL. Downloaded on September 22,2023 at 00:11:30 UTC from IEEE Xplore. Restrictions apply.

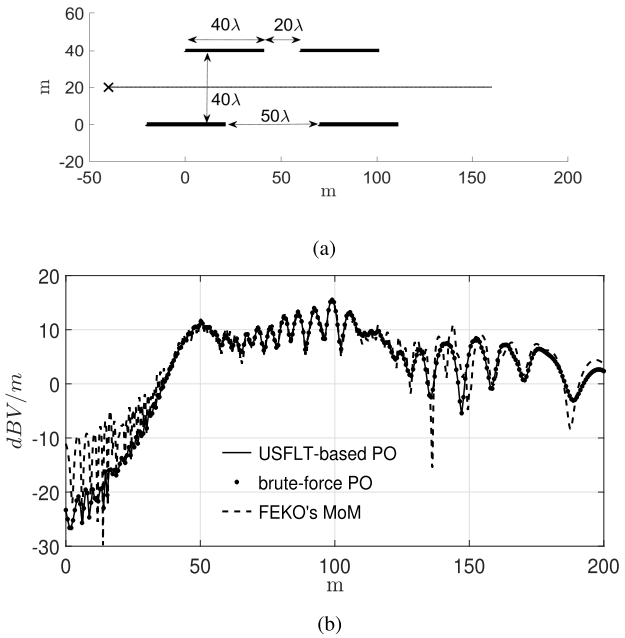


Fig. 10. (a) Radio propagation in a canyon with Tx position (cross) and Rx path (solid line). (b) Amplitude of the scattered electric fields obtained with the spatial-domain integration (dots), with the fast method (solid line), and with FEKO's MoM.

in an urban environment modeled with large planar facets. The geometry of this scenario is illustrated in Fig. 10(a) and resembles a narrow urban street consisting of a collection of square facets each of size 40λ, i.e., roughly 6 m wide at 1.8 GHz. A vertically polarized transmitter (Tx), modeled again with a point source, is positioned at one end of the canyon and illuminates all plates in line of sight. One seeks to evaluate the scattered electric field along a straight observation path lying in the middle of the street. Iterative implementation of the PO is used here to include second-order scattering interactions, i.e., double bounces. The magnitude of the scattered field, expressed here in dBV/m units, computed with the fast spectral-domain method or a direct spatial-domain integration, is plotted in Fig. 10(b) alongside full-wave simulations obtained with the MoM solver of FEKO [33]. In this example, the USFLT-based method is used only to accelerate the double-bounce PO interactions that are found to be the most time-consuming operations since the computation time of the brute force integration grows as N^2. One can see a good agreement (two digits of accuracy) between the fields computed with the two methods. The computation times for the fast and the brute-force methods are 1 s and 15 min, respectively. The MoM simulations, plotted additionally in Fig. 10(b), indicate that the scattered field is accurately estimated as long as the receiver remains between the plates where the specular reflections are stronger but starts to diverge at the beginning and at the end of the observation path where singular currents on the plate edges contribute more significantly.

V. Conclusion

We have presented a fast method for the computation of radiated fields over an observation plate from current distributions given on a source plate, which can be tilted w.r.t. each other. The method uses a generalization of the NFFT, called the USFLT [29], to rapidly perform the direct and inverse transformations between the spatial and spectral domains. More precisely, the USFLT allows the rapid computation of discrete Fourier transforms from or at irregularly spaced and complex-valued spectral samples, which results from the numerical evaluation of the spectral-to-spatial transform using a contour deformation technique to circumvent the free-space singularity on the real axis. This is achieved by either redistributing the irregular and complex-valued samples on a regular grid in the real plane or by interpolating from these grids at samples in the complex plane.

As an alternative to the C-FFT [12], the USFLT can be used to rapidly compute the Fourier transforms of the singular functions appearing in the simulation of printed circuits above layered media using the method of moments, e.g., to perform fast matrix–vector products as part of an iterative solver [7] or accelerate the computation of the reaction integrals between macrobasis functions [12]. The USFLT presents, however, the advantage of requiring only a single FFT per transformation and, thus, offers lower computational overheads. Latter studies should focus on the use of the type 3 USFLT, which is suited to both irregular spatial and spectral samples [29] and enables the handling of problems with arbitrary planar geometry without the need for extra interpolation/aggregation steps between the spatial grid and the irregular mesh representing the surface of the scatterer.

Finally, we have shown that the fast USFLT-based method is well suited to accelerate the computation of radiation integrals when the observation plate is tilted w.r.t. the source plate. Indeed, as long as the plates stand in each other intermediate fields, typically from one plate size away, the computation cost of the gridding step remains similar to or lower than that of the FFTs. Hence, when dealing with problems involving electrically large planar structures, the proposed approach is expected to be more efficient than those based on the fast multipole method [4], which requires the fast computation of a translation function for the interactions between each pair of subdomains [23], [31], but also than those based on the adaptive integral method [3] that uses 3-D FFTs.

Appendix
Parameterization for Gaussian Windows

Throughout this article, we consider 2-D Gaussian functions of variances μ_x and μ_y defined by

$$\tilde{\psi}\left(k_{xr}, k_{yr}\right) = \frac{2\pi}{\sqrt{\mu_x \mu_y}}\, e^{-k_{xr}^2/(2\mu_x)}\, e^{-k_{yr}^2/(2\mu_y)} \tag{32}$$

with spatial counterpart given by $\psi(x, y) = e^{-2\mu_x x^2 - 2\mu_y y^2}$. As described in III-C, the window functions $\tilde{\psi}$ in both types of USFLT are evaluated at complex arguments. Hence, the Gaussian functions $\tilde{\psi}$ can be expanded into

$$\tilde{\psi}\left(k_x, k_y\right) = \frac{2\pi}{\sqrt{\mu_x \mu_y}}\, e^{-jk_{xr}k_{xi}/\mu_x}\, e^{-jk_{yr}k_{yi}/\mu_y} \times\, e^{-\left(k_{xr}^2 - k_{xi}^2\right)/(2\mu_x)}\, e^{-\left(k_{yr}^2 - k_{yi}^2\right)/(2\mu_y)}. \tag{33}$$

Authorized licensed use limited to: Univ Catholique de Louvain/UCL. Downloaded on September 22,2023 at 00:11:30 UTC from IEEE Xplore. Restrictions apply.

The factorization of the exponentials in (33) indicates that, contrary to (32) for purely real arguments, the function $\tilde{\psi}$ oscillates and decreases more slowly when evaluated in the complex plane. Let us now briefly analyze the errors appearing in the numerical evaluation of the spectral integrals (15) and (19) with complex samples $(k_{x,p}, k_{y,p})$ for this particular choice of window functions $\tilde{\psi}$. Given a set of oversampling factors $\bar{\nu}_x$ and $\bar{\nu}_y$ fixing the sampling rates through $\Delta\bar{k}_x = 2\pi/(\bar{\nu}_x L_x)$ and $\Delta\bar{k}_y = 2\pi/(\bar{\nu}_y L_y)$, the discretization errors can be controlled by parameterizing the variances with [29]

$$\mu_x = \frac{-\ln\epsilon}{\bar{\nu}_x(\bar{\nu}_x - 1)L_x^2} + \frac{k_{xim}}{2L_x(\bar{\nu}_x - 1)} \tag{34}$$

where one notes an extra term proportional to the maximum imaginary part k_{xim} taken by the complex spectral samples $k_{x,p}$. Hence, one must select a variance slightly larger for complex samples than for real ones. Then, the discrete convolutions (24) and (25) can be truncated to terms of indices p or q satisfying $|\bar{k}_{xr,p} - q_x\Delta\bar{k}_x| \leq \bar{k}_{xm}$ with the truncation limit $\bar{k}_{xm}$ given by [29]

$$\bar{k}_{xm} = 2\left(\mu_x^2 L_x^2 - 2\mu_x \ln\epsilon\right)^{1/2}. \tag{35}$$

This also implies that the Fourier integrals (15) and (19) must be truncated at $k_{xm} + \bar{k}_{xm}$ with $k_{xm} = \max|k_{xr,p}|$ being the maximum value among the spectral samples $k_{xr,p}$.

ACKNOWLEDGMENT

This research was carried out within the research project B-WARE funded by the WB-Health Program of the Walloon Region, the BESTCOM interuniversity Belgian Research Program, and the research project MACHAON funded by F.R.S.-FNRS.

REFERENCES

[1] E. B. Joy and D. Paris, "Spatial sampling and filtering in near-field measurements," *IEEE Trans. Antennas Propag.*, vol. AP-20, no. 3, pp. 253–261, May 1972.

[2] A. D. Yaghjian, "An overview of near-field antenna measurements," *IEEE Trans. Antennas Propag.*, vol. AP-34, no. 1, pp. 30–45, Jan. 1986.

[3] E. Bleszynski, M. Bleszynski, and T. Jaroszewicz, "AIM: Adaptive integral method for solving large-scale electromagnetic scattering and radiation problems," *Radio Sci.*, vol. 31, no. 5, pp. 1225–1251, Sep./Oct. 1996.

[4] N. Engheta, W. D. Murphy, V. Rokhlin, and M. S. Vassiliou, "The fast multipole method (FMM) for electromagnetic scattering problems," *IEEE Trans. Antennas Propag.*, vol. 40, no. 6, pp. 634–641, Jun. 1992.

[5] X.-C. Nie, L.-W. Li, and N. Yuan, "Precorrected-FFT algorithm for solving combined field integral equations in electromagnetic scattering," *J. Electromagn. Waves Appl.*, vol. 16, no. 8, pp. 574–577, 2002.

[6] B. J. Fasenfest, F. Capolino, D. R. Wilton, D. R. Jackson, and N. J. Champagne, "A fast MoM solution for large arrays: Green's function interpolation with FFT," *IEEE Antennas Wireless Propag. Lett.*, vol. 3, pp. 161–164, 2004.

[7] S. Hubert, S. N. Jha, and C. Craeye, "Analysis of large nonregular printed scatterers using the contour-FFT," *IEEE Trans. Antennas Propag.*, vol. 66, no. 11, pp. 6115–6127, Nov. 2018.

[8] A. Dutt and V. Rokhlin, "Fast Fourier transforms for nonequispaced data," *SIAM J. Sci. Comput.*, vol. 14, no. 6, pp. 1368–1393, 1993.

[9] A. Capozzoli, C. Curcio, A. Liseno, and G. Toso, "Fast, phase-only synthesis of aperiodic reflectarrays using NUFFTs and CUDA," *Prog. Electromagn. Res. A*, vol. 156, pp. 83–103, 2016.

[10] T. K. Sarkar and A. Taaghol, "Near-field to near/far-field transformation for arbitrary near-field geometry utilizing an equivalent electric current and MoM," *IEEE Trans. Antennas Propag.*, vol. 47, no. 3, pp. 566–573, Mar. 1999.

[11] P. C. Clemmow, *The Plane Wave Spectrum Representation of Electromagnetic Fields*. New York, NY, USA: Pergamon Press, 1966.

[12] S. N. Jha and C. Craeye, "Contour-FFT based spectral domain MBF analysis of large printed antenna arrays," *IEEE Trans. Antennas Propag.*, vol. 62, no. 11, pp. 5752–5764, Nov. 2014.

[13] L. R. Rabiner, R. W. Schafer, and C. M. Rader, "The chirp z-transform," *IEEE Trans. Audio Electroacoust.*, vol. AU-17, no. 2, pp. 86–92, Jun. 1969.

[14] Y. L. Li, C. H. Liu, and S. J. Franke, "Adaptive evaluation of the sommerfeld-type integral using the chirp z-transform," *IEEE Trans. Antennas Propag.*, vol. 39, no. 12, pp. 1788–1791, Dec. 1991.

[15] H. Ostner, J. Detlerfsen, and D. R. Jackson, "Radiation from one-dimensional dielectric leaky-wave antennas," *IEEE Trans. Antennas Propag.*, vol. 43, no. 4, pp. 331–339, Apr. 1995.

[16] I. Kavanagn and C. Brennan, "Full wave indoor propagation modelling using the volume integral equation," *Prog. Electromagn. Res. B*, vol. 84, pp. 171–187, 2019.

[17] E. G. Papkelis *et al.*, "A radio-coverage prediction model in wireless communication systems based on physical optics and the physical theory of diffraction [wireless corner]," *IEEE Antennas Propag. Mag.*, vol. 49, no. 2, pp. 156–165, Apr. 2007.

[18] C. Craeye, "On the transmittance between OAM antennas," *IEEE Trans. Antennas Propag.*, vol. 64, no. 1, pp. 336–339, Jan. 2016.

[19] K. Matsushima, H. Schimmel, and F. Wyrowski, "Fast calculation method for optical diffraction on tilted planes by use of the angular spectrum of plane waves," *J. Opt. Soc. Amer. A, Opt. Image Sci.*, vol. 20, no. 9, pp. 1755–1762, Sep. 2003.

[20] Y. Xiao *et al.*, "Nonuniform fast Fourier transform method for numerical diffraction simulation on tilted planes," *J. Opt. Soc. Amer. A, Opt. Image Sci.*, vol. 33, no. 10, pp. 2027–2033, Oct. 2016.

[21] L. Onural, "Exact solution for scalar diffraction between tilted and translated planes using impulse functions over a surface," *J. Opt. Soc. Amer. A, Opt. Image Sci.*, vol. 28, no. 3, pp. 290–295, Mar. 2011.

[22] L. Onural, A. Gotchev, H. M. Ozaktas, and E. Stoykova, "A survey of signal processing problems and tools in holographic three-dimensional television," *IEEE Trans. Circuits Syst. Video Technol.*, vol. 17, no. 11, pp. 1631–1646, Nov. 2007.

[23] W. C. Chew, J. M. Jin, and E. Michielssen, *Fast and Efficient Algorithms in Computational Electromagnetics*. Norwood, MA, USA: Artech House, 2001.

[24] Q. Gueuning, C. Craeye, and C. Oestges, "Sampling rules for an inhomogeneous plane-wave representation of scattered fields," *IEEE Trans. Antennas Propag.*, vol. 67, no. 3, pp. 1697–1708, Mar. 2019.

[25] J. A. Stratton, *Electromagnetic Theory*. New York, NY, USA: McGraw-Hill, 1941.

[26] Wikipedia. *Convolution Theorem*. Accessed: Apr. 26, 2022. [Online]. Available: https://en.wikipedia.org/wiki/Convolution_theorem

[27] K. A. Michalski and J. R. Mosig, "Efficient computation of Sommerfeld integral tails—Methods and algorithms," *J. Electromagn. Waves Appl.*, vol. 30, no. 3, pp. 281–317, Feb. 2016.

[28] W. C. Chew, *Waves and Fields in Inhomogenous Media*. Hoboken, NJ, USA: Wiley, 1999.

[29] F. Andersson, "Algorithms for unequally spaced fast Laplace transforms," *Appl. Comput. Harmon. Anal.*, vol. 35, no. 3, pp. 419–432, Nov. 2013.

[30] C. Craeye, "A fast impedance and pattern computation scheme for finite antenna arrays," *IEEE Trans. Antennas Propag.*, vol. 54, no. 10, pp. 3030–3034, Oct. 2006.

[31] O. Ergul and L. Gurel, "Optimal interpolation of translation operator in multilevel fast multipole algorithm," *IEEE Trans. Antennas Propag.*, vol. 54, no. 12, pp. 3822–3826, Dec. 2006.

[32] Q. Gueuning, S. Hubert, C. Craeye, and C. Oestges, "Error model for contour-FFT evaluation of the free-space on-plane Green's function," in *Proc. URSI Int. Symp. Electromagn. Theory (EMTS)*, Espoo, Finland, Aug. 2016, pp. 312–314.

[33] *FEKO*. [Online]. Accessed: Apr. 26, 2022. Available: http://www.feko.info

[34] *MATLAB*. [Online]. Accessed: Apr. 26, 2022. Available: http://www.mathworks.com

[35] *Fastest Fourier Transform in the West (FFTW)*. Accessed: Apr. 26, 2022. [Online]. Available: http://www.fftw.org

Authorized licensed use limited to: Univ Catholique de Louvain/UCL. Downloaded on September 22,2023 at 00:11:30 UTC from IEEE Xplore. Restrictions apply.



Quentin Gueuning received the Ph.D. degree from the Université Catholique de Louvain (UCLouvain), Ottignies-Louvain-la-Neuve, Belgium, in 2019.

Since 2019, he has been a Research Associate with the Cavendish Astrophysics Group, University of Cambridge, Cambridge, U.K. His research interests include fast computational methods and asymptotic high-frequency theories, electromagnetic theory, mutual coupling, array and antenna design and measurements, telescope calibration, and channel characterization.



Christophe Craeye (Senior Member, IEEE) was born in Belgium in 1971. He received the Electrical Engineering and B.Phil. degrees and the Ph.D. degree in applied sciences from the Université Catholique de Louvain (UCL), Ottignies-Louvain-la-Neuve, Belgium, in 1994 and 1998, respectively.

From 1994 to 1999, he was a Teaching Assistant with UCL and carried out research on the radar signature of the sea surface perturbed by rain, in collaboration with NASA and the European Space Agency (ESA). From 1999 to 2001, he was a Post-Doctoral Researcher with the Eindhoven University of Technology, Eindhoven, The Netherlands. He was with the University of Massachusetts Amherst, Amherst, MA, USA, in 1999. He was with the Netherlands Institute for Research in Astronomy, Dwingeloo, The Netherlands, in 2001. In 2002, he started the antenna research activity at UCL, where he is currently a Professor. He was with the Astrophysics and Detectors Group, University of Cambridge, Cambridge, U.K., in 2011. His research was funded by the Region Wallonne, the European Commission, ESA, the Fonds National de la Recherche Scientifique (FNRS), and UCL. His current research interests include mutual coupling, finite antenna arrays, wideband antennas, small antennas, metamaterials, fast physical optics, and numerical methods for fields in periodic media with applications to communication and sensing systems.

Dr. Craeye received the 2005–2008 Georges Vanderlinden Prize from the Belgian Royal Academy of Sciences in 2009. He was an Associate Editor of the IEEE TRANSACTIONS ON ANTENNAS AND PROPAGATION from 2004 to 2010 and the IEEE ANTENNAS AND WIRELESS PROPAGATION LETTERS from 2011 to 2017.



Claude Oestges (Fellow, IEEE) received the M.Sc. and Ph.D. degrees in electrical engineering from the Université Catholique de Louvain (UCLouvain), Ottignies-Louvain-la-Neuve, Belgium, in 1996 and 2000, respectively.

In January 2001, he joined the Smart Antennas Research Group (Information Systems Laboratory), Stanford University, Stanford, CA, USA, as a Post-Doctoral Scholar. From January 2002 to September 2005, he was with the Microwave Laboratory, UCLouvain, as a Post-Doctoral Fellow of the Belgian Fonds de la Recherche Scientifique (FRS-FNRS). He is currently a Full Professor with the Electrical Engineering Department, Institute for Information and Communication Technologies, Electronics and Applied Mathematics (ICTEAM), UCLouvain. He is the author or a coauthor of three books and more than 200 journal articles and conference communications.

Dr. Oestges was a recipient of the 1999-2000 IET Marconi Premium Award and the IEEE Vehicular Technology Society Neal Shepherd Awards in 2004 and 2012. He was the Chair of COST Action CA15104 IRACON from 2016 to 2020.

Authorized licensed use limited to: Univ Catholique de Louvain/UCL. Downloaded on September 22,2023 at 00:11:30 UTC from IEEE Xplore. Restrictions apply.